ARTICLE   OPEN

Charge carrier mobilities of organic semiconductors: ab initio simulations with mode-specific treatment of molecular vibrations

Sebastian Hutsch[1], Michel Panhans[1] and Frank Ortmann [ID][1] ✉

The modeling of charge transport in organic semiconductors usually relies on the treatment of molecular vibrations by assuming a certain limiting case for all vibration modes, such as the dynamic limit in polaron theory or the quasi-static limit in transient localization theory. These opposite limits are each suitable for only a subset of modes. Here, we present a model that combines these different approaches. It is based on a separation of the vibrational spectrum and a quantum-mechanical treatment in which the slow modes generate a disorder landscape, while the fast modes generate polaron band narrowing. We apply the combined method to 20 organic crystals, including prototypical acenes, thiophenes, benzothiophenes, and their derivatives. Their mobilities span several orders of magnitude and we find a close agreement to the experimental mobilities. Further analysis reveals clear correlations to simple mobility predictors and a combination of them can be used to identify high-mobility materials.

INTRODUCTION

Organic semiconductors are used in various electronic devices, including organic field effect transistors[1–4], organic photovoltaics[5–7], and organic light emitting diodes[8–10]. Many applications rely on charge-transport processes and the charge-carrier mobility is an important property affecting the device performance. This is a strong motivation to improve the understanding of charge transport in organic semiconductors and a variety of methods have been suggested[11–24]. The modeling of charge transport, however, remains challenging, because the electrons couple strongly to the molecular vibrations. This coupling, known as electron-phonon coupling (EPC), prevents a straightforward analytical treatment of the electronic and vibrational degrees of freedom. Recent improvements in computational methods allow to model the charge transport numerically while propagating vibrations semiclassically[22,25]. Although these numerical approaches are generally promising, performing them fully based on ab initio simulations is still expensive for the screening of new materials. Therefore, the number of materials that can be studied and compared simultaneously remain limited. To tackle the complexity, the exploitation of analytical limits can improve the computational efficiency and, more importantly, may push the microscopic understanding of the carrier mobility forward. One of the first classes of analytical models that go beyond a semi-classical treatment of nuclei are polaron theories[11,13,26], which describe the formation of the polaron, a charge carrier accompanied by dynamic molecular vibrations. However, the polaronic character is assumed to be weak for the slow, thermally populated vibrations[27,28], which often show large EPC. Transient localization theory, initially developed by Troisi, Fratini, Ciuchi, Mayou, and colleages[21,29,30], on the other hand focusses on these strongly-coupling low-frequency vibrations, which tend to localize the electronic wave packets in an electronic disorder landscape that is static at small times. At longer times, however, the inevitable motion of the low-frequency modes sets in, presumably lifting this effect – hence the name transient localization (TL). The quasi-static

approximation inherent to TL is successful because a strong contribution to the EPC stems from thermally activated low-frequency vibrations. Still, the fast intramolecular high-frequency vibrations, which must not be modeled quasi-statically but generate coherent polaron dressing, also show a large EPC and should not be neglected, which eventually implies a separation of the vibrational mode spectrum[31–33].

Here, we present an approach to simulate coherent electronic transport, which combines the quasi-static treatment of slow modes in the TL approach with the polaronic treatment of the high-frequency vibrations from polaron approaches (cf. Fig. 1a for a prototypical vibrational spectrum of an OSC material). The EPC of slow low-frequency vibrations generates quasi-static disorder (Fig. 1b, blue), while the EPC of fast high-frequency vibrations generates polaron narrowing (orange). Using the combined model, we calculate the hole mobilities via simulations for extended 3D system utilizing linear-scaling quantum transport methods[34,35]. To assess the predictive capability of the approach statistically, it is applied to 20 prototypical organic crystals with known experimental mobilities that span two orders of magnitude. We find a close agreement between the mobilities obtained with this approach and the experimental mobility trend. Finally, the validity of simplified mobility predictors like reorganization energies, transfer integrals, and dimensionality is analyzed and a combination of easy-to-compute predictors for fast mobility estimates is found, which is superior to their single predictor components and can be useful in machine-learning schemes to find high-mobility organic semiconductors.

RESULTS AND DISCUSSION

Combination of the quasi-static and polaronic treatment

Organic molecules and their crystals show a rich vibrational spectrum. In Fig. 1a, this is illustrated for a DNTT crystal built by a supercell cell with 8 molecules. The vibration frequencies are spread over two orders of magnitude, ranging from ~10 cm^{-1} to

[1]School of Natural Sciences, Department of Chemistry, Technische Universität München, Garching b. München, Germany. ✉email: frank.ortmann@tum.de
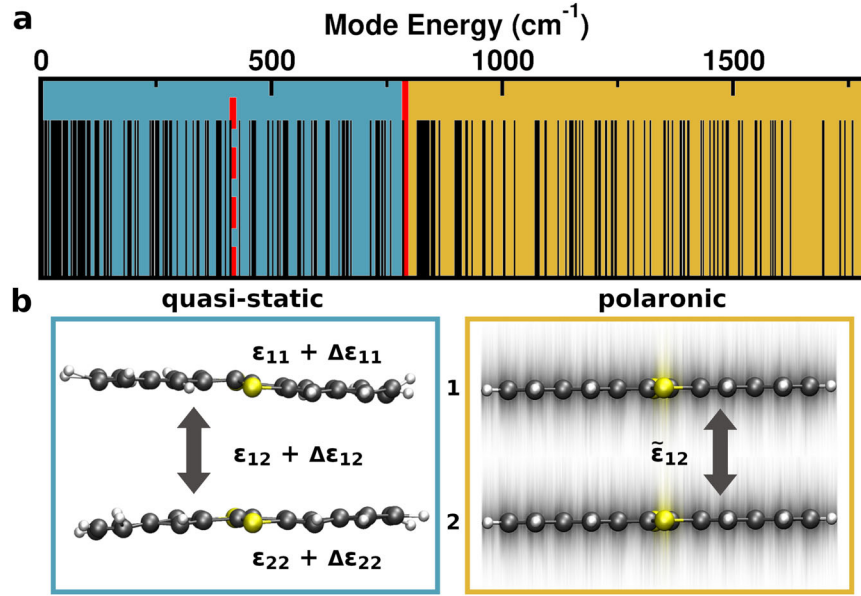
Fig. 1 Separation of quasi-static and polaronic vibration modes. a Mode spectrum of a DNTT crystal. The separating energy (the maximum transfer integral ε_{MN}^{max}) is highlighted as red vertical bar. Modes with lower energy are treated in the quasi-static limit (blue), modes with larger energy in the polaronic limit (orange). As a reference, twice the thermal energy $2k_BT$ at room temperature is highlighted as dashed red bar. **b** The quasi-static treatment generates static disorder in the transfer integrals ε_{MN} and onsite energies ε_{MN}. The polaronic treatment generates a narrowing of the electronic transfer integrals ε_{MN}.

above 1000 cm^{-1}. To account for this wide range, the slow modes are modeled within the quasi-static limit of TL (blue) and enter via their instantaneous configuration, while the faster high-frequency modes enter in the dynamic polaronic limit (yellow), integrating all configurations. Both treatments influence the electronic energies, but in a different fashion as we will elucidate in the following.

The starting point for the calculations and mode separations is the Holstein-Peierls-Hamiltonian[11,36], which includes the electronic, vibrational, and EPC contributions

$$
\begin{aligned}
H &= H_{el} + H_{el-ph} + H_{ph} \\
&= \sum_{MN} \varepsilon_{MN} a_M^\dagger a_N \\
&\quad + \sum_{MN} \sum_Q \hbar\omega_Q g_{MN}^Q \left(b_Q^\dagger + b_{-Q}\right) a_M^\dagger a_N \\
&\quad + \sum_Q \hbar\omega_Q \left(b_Q^\dagger b_Q + \frac{1}{2}\right)
\end{aligned}
\tag{1}
$$

in a mixed representation with the electronic operators a_M ($a_M^\dagger$), the onsite-energies ε_{MM} and transfer integrals ε_{MN}. The phonon operators b_Q ($b_Q^\dagger$) are used with $Q = (\lambda, \mathbf{q})$ and λ being the mode index and $\mathbf{q}$ the wave vector. The coupling between the phonons and electrons is described by the linear EPC constants g_{MN}^Q, including local coupling (coupling to the onsite-energies) for $M = N$ and nonlocal coupling (coupling to the transfer integrals) for $M \neq N$. To calculate the charge-carrier mobility by an electronic quantum-transport approach, the Holstein-Peierls-Hamiltonian in Eq. (1) will be reduced to a completely electronic Hamiltonian. To this end, the impact of the phonon contributions to the electronic energies in the quasi-static and polaronic limit will be analytically pre-evaluated. We briefly summarize the essential steps of the derivation here, while more details can be found in Supplementary Note 1. The slow modes are assumed to generate a (quasi-)static disorder $\Delta\varepsilon_{MN}$ in the electronic energies due to their instantaneously frozen configuration[31]. With a Gaussian distribution of the disordered energies $\varepsilon_{MN} + \Delta\varepsilon_{MN}$ around ε_{MN}, the

variance σ_{MN}^2 of $\Delta\varepsilon_{MN}$ can be evaluated to[37]

$$
\sigma_{MN}^2 = \sum_Q^{slow} (\hbar\omega_Q)^2 \left|g_{MN}^Q\right|^2 (1 + 2N_Q),
\tag{2}
$$

with the Bose-Einstein distribution $N_Q = \left(e^{\hbar\omega_Q/k_BT} - 1\right)^{-1}$, the Boltzmann constant k_B, and absolute temperature T.

In contrast to the *slow* modes, the *fast* modes are treated here by a Lang-Firsov-transformation[13,38] of Eq. (1). As a result, the transfer integrals ε_{MN} are reduced by a narrowing factor f_{nar} and the onsite-energies ε_{MM} are shifted by the polaron binding (relaxation) energy $E_{pol} = \sum_Q^{fast} \hbar\omega_Q |g_{MM}^Q|^2$ as [13]

$$
\begin{aligned}
\tilde{\varepsilon}_{MN} &= \varepsilon_{MN} f_{nar}, \quad \text{for}(M \neq N) \\
f_{nar} &= \exp\left(-\frac{1}{2}\sum_Q^{fast}(1 + 2N_Q)G_{MN}^Q\right), \\
G_{MN}^Q &= \left|g_{MM}^Q - g_{NN}^Q\right|^2 + \sum_{K \neq M}\left|g_{MK}^Q\right|^2 + \sum_{K \neq N}\left|g_{NK}^Q\right|^2, \\
\tilde{\varepsilon}_{MM} &= \varepsilon_{MM} - E_{pol}.
\end{aligned}
\tag{3}
$$

In case of equal molecules at each site M ($g_{MM}^Q = g_{NN}^Q$ for all M and N), E_{pol} is an energetic shift that applies to all sites and can be disregarded.

By combining Eq. (3) and Eq. (2) and Eq. (1), the Holstein-Peierls-Hamiltonian is reduced to the effective electronic Hamiltonian:

$$
\begin{aligned}
\overline{H} &= \sum_{MN} \overline{\varepsilon}_{MN} a_M^\dagger a_N, \\
\overline{\varepsilon}_{MM} &= \varepsilon_{MM} + \Delta\varepsilon_{MM}, \\
\overline{\varepsilon}_{MN} &= (\varepsilon_{MN} + \Delta\varepsilon_{MN})f_{nar} \quad \text{for}(M \neq N)
\end{aligned}
\tag{4}
$$

and $\Delta\varepsilon_{MN}$ follows a Gaussian distribution according to Eq. (2). Although in real systems there is no sharp transition between slow and fast modes, the separation has to be numerically performed with a distinct cut-off criterion. Here, we chose the maximum between twice the thermal energy[32] (red dotted bar in Fig. 1) and the maximum transfer integral ε_{MN}^{max} (red bar in Fig. 1) as a

separation criterion, i.e.,

$$\hbar\omega_{slow} \leq \max\left(\varepsilon_{MN}^{max}, 2k_BT\right) < \hbar\omega_{fast}. \quad (5)$$

This simultaneously ensures that the thermally activated low-frequency vibrations are treated quasi-statically in the case of small transfer integrals, while only the fast high-frequency vibrations are treated in the polaron limit in the case of large transfer integrals.

Calculation of the charge-carrier mobility

The calculation of the charge-carrier mobility is based on linear-response theory within the Kubo formalism[39]. This can be evaluated in the presence of disorder $\bar{\varepsilon}_{MN}$ (cf. Eq. (4)). Since the disorder landscape changes on the effective time-scale of the slow quasi-static modes τ_{slow}, this short-time behavior is lifted at longer times than τ_{slow}, which thus acts as a decoherence time. With this in mind, the TL mobility is calculated as[30]

$$\mu = \frac{e}{2k_BT(\tau_{slow}^2)}\int_0^\infty e^{-\frac{t}{\tau_{slow}}}\langle\Delta X^2(t)\rangle dt = \frac{e}{2k_BT}\frac{L_{loc}^2}{\tau_{slow}}, \quad (6)$$

$L_{loc}^2 = \frac{1}{\tau_{slow}}\int_0^\infty e^{-\frac{t}{\tau_{slow}}}\langle\Delta X^2(t)\rangle dt$ is the squared localization length – it measures the average spread of the wave-packet up to the time τ_{slow} and is derived from the thermally averaged, time-resolved quantum spread $\langle\Delta X^2(t)\rangle$. While there exist simplified versions to compute L_{loc} for 2D systems by a direct diagonalization[40] of the disordered Hamiltonian similar to Eq. (4), we calculate the localization length by calculating the time-resolved quantum spread $\langle\Delta X^2(t)\rangle$ via propagation in real-space 3D systems. In this way, we include the effect of possible 3D percolation pathways in the sample. The thermally averaged quantum spread is calculated as

$$\langle\Delta X^2(t)\rangle = \int\frac{dE\,f(E)[1-f(E)]DOS(E)\Delta X^2(E,t)}{N_0}, \quad (7)$$

with the Fermi-Dirac distribution $f(E) = 1/(e^{(E-\zeta)/k_BT}+1)$ and the charge-carrier concentration $N_0 = \int dE\,f(E)DOS(E)$. The chemical potential ζ is chosen such that the charge-carrier concentration equals $N_0 = 0.001$ for all materials. More details on the calculation of the time- and energy-resolved quantum spread $\Delta X^2(E,t)$ can be found in the methods section. With the chosen system size of approximately 12 million sites, a single transport simulation requires only about 2500 CPUh and can be readily performed in parallel on any computer cluster.

Transport parameters

Regarding EPC parameters, we distinguish between three types of EPC, which are visualized in Fig. 2 for DNTT and briefly introduced here. There are (i) the local terms g_{MM}^Q (Fig. 2a). It is the coupling of molecular vibrations to the onsite-energy of a single molecule M (top). The local coupling covers the full range of vibration frequencies (bottom), necessitating a separation into quasi-static contributions (blue) and polaronic contributions (orange). The resulting polaronic narrowing factor is, in average over the studied materials, $\bar{f}_{nar} = 0.6$. (ii) The nonlocal EPC g_{MN}^Q (Fig. 2b) is the coupling to the transfer integrals mediating between sites M and N (top). It is clearly dominated by low-frequency vibrations, leading to a quasi-static disorder landscape in the transfer integrals[21,40]. (iii) The environmental coupling $g_{MM}^{Q,CF}$ (Fig. 2c) is the coupling of the crystal vibrations to the electrostatic interaction energy E_{CF} between the charge carrier at site M and the crystal field of the surrounding molecules. Similar to the
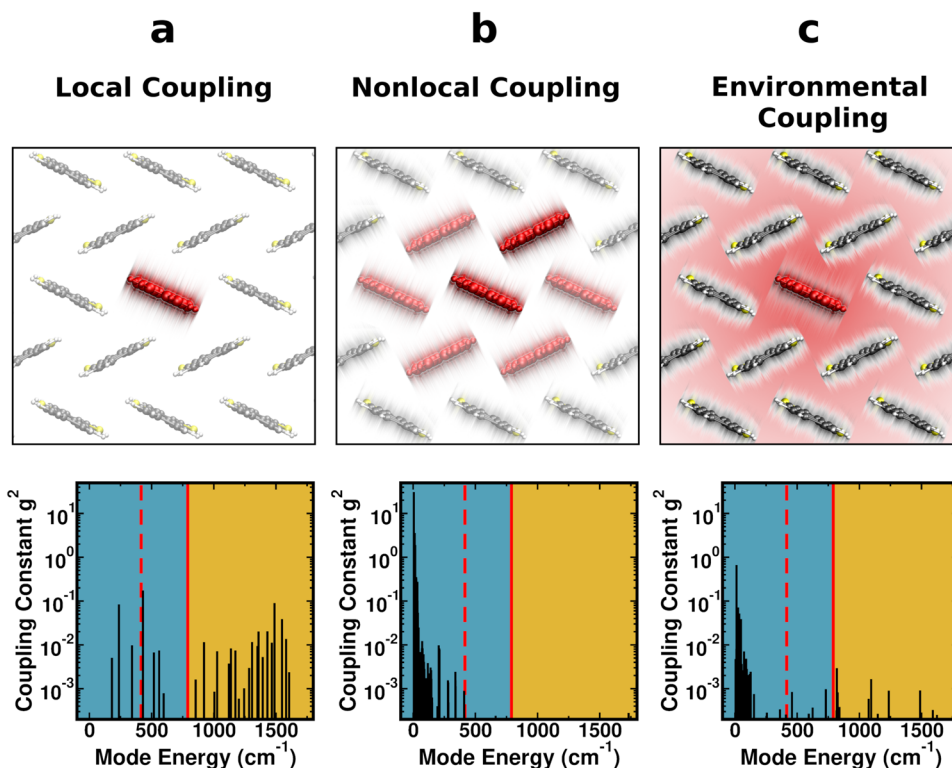

Fig. 2 Mode-resolved EPC. Top: three types of EPC implemented in this approach: **a** local coupling to the onsite energies, **b** nonlocal coupling to the transfer integrals between two molecules and **c** environmental coupling to the electrostatic crystal field. Bottom: mode-resolved squared EPC constant g^2 for the three types of coupling of the exemplary molecule DNTT. The energy scale of transport ε_{MN}^{max} is indicated as red vertical bar. The modes that are treated quasi-statically are highlighted in blue, while the ones that are treated with the polaron approach are highlighted in orange. Twice the thermal energy $2k_BT$ at room temperature, which is the separating energy for small transfer integrals, is highlighted as dashed red bar.

Table 1. Analyzed materials and their properties.

Material	$\mu_{exp}\left(\frac{cm^2}{Vs}\right)$	$\mu_{sim}\left(\frac{cm^2}{Vs}\right)$	$\mu_{sim}^{APT}\left(\frac{cm^2}{Vs}\right)$	ε_{MN}^{max} (meV)	σ_{MN} (meV)	σ_{MM} (meV)	σ_{env} (meV)	d_{mol} (Å)	δ_{dim}	τ_{slow} (fs)	Λ (meV)
Anthracene	2.9	2.7	6.2	46	24	0	25	6.0	1.52	185	141
BB-PTA	0.5	0.25	0.25	180	82	110	20	3.9	1.04	180	243
C10-DNBDT	12.1	14.2	14.2	49	14	25	16	6.1	1.97	201	89
C10-DNTT	11.0	12.1	12.1	70	12	31	15	6.0	1.81	143	136
DBTDT	1.8	2.0	4.5	49	13	23	21	5.0	1.66	165	103
DNTT	8.3	3.5	7.2	98	19	30	24	6.2	1.42	238	134
DPA	3.7	4.8	10.4	32	13	5	19	8.6	1.70	196	154
DT-TTF	1.4	0.64	0.64	55	89	45	27	4.0	1.77	203	233
Durene	5.0	8.6	8.6	74	45	7	19	5.7	1.86	116	193
HM-TTF	10.0	8.3	19.6	111	38	53	23	6.4	1.42	146	218
Naphthalene	1.0	2.7	4.7	42	25	0	25	5.9	1.48	139	189
NTMTI	0.37	0.33	0.36	31	16	45	16	3.2	1.46	61	226
Pentacene	5.0	2.8	10.3	77	30	8	24	4.8	1.80	156	95
Picene	9.0	15.5	15.5	79	14	35	22	6.1	1.88	100	190
PMSB	0.17	0.07	0.07	44	26	78	25	4.8	1.30	198	408
Rubrene	15.3	12.4	12.6	104	43	30	16	7.2	1.24	113	160
Tetracene	2.4	2.9	3.1	79	41	5	32	4.8	1.45	267	116
TIPS-Pentacene	2.7	3.0	3.1	52	34	19	18	7.6	1.14	248	138
TTF-α	1.2	1.0	1.1	122	74	73	27	4.0	1.23	96	288
TTF-β	0.23	0.76	0.89	50	65	39	26	5.5	1.68	164	288

Presented are the experimental mobility μ_{exp}, simulated mobility μ_{sim}, and the simulated mobility μ_{sim}^{APT} using all positive signs for the transfer integrals. Further, the bare maximum transfer integral ε_{MN}^{max}, the nonlocal disorder in the same σ_{MN}, the local disorder σ_{MM}, and environmental disorder σ_{env} are collected. We further present the center-of-mass distance between the molecules d_{mol} connected by the largest transfer integral, the dimensionality factor δ_{dim} and relaxation time τ_{slow}. Finally, the reorganization energy Λ as a convenient measure of the local coupling is shown, albeit not directly used in the simulations. It enters via the local disorder σ_{MM} and narrowing factor f_{nar} (not shown, with an average value of $\bar{f}_{nar} = 0.6$). References to the experimental crystal structures and mobilities can be found in Supplementary Table 2.
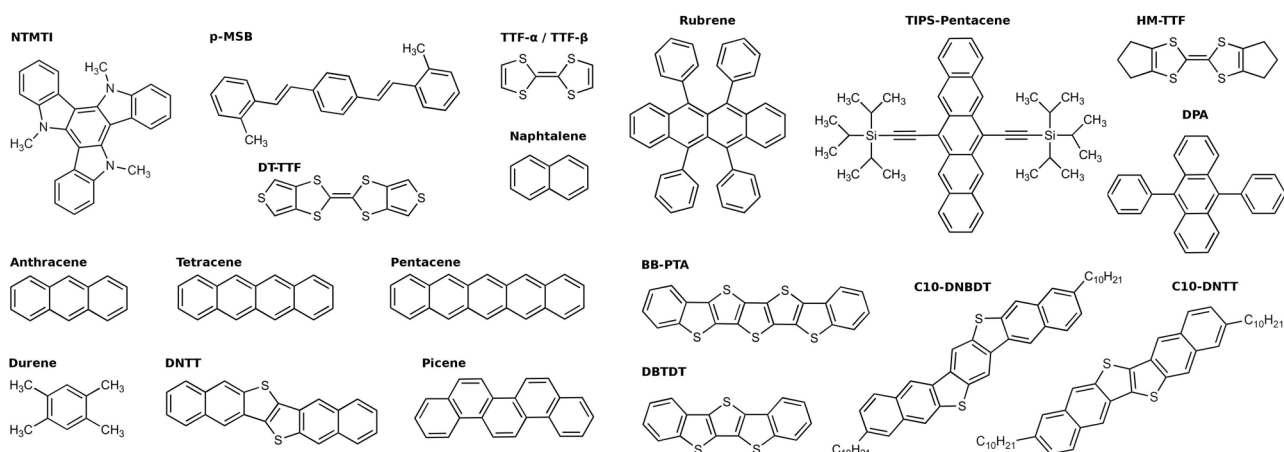

Fig. 3 The 20 materials studied with the combined approach. They were chosen to cover a wide range of experimental mobilities. For the TTF molecule, we studied two known crystal structures. References to the studied crystal structures can be found in Supplementary Table 2.

nonlocal coupling it is dominated by low-frequency vibrations, generating quasi-static disorder in the onsite energies. The environmental coupling is found to contribute only little to the disorder compared to the nonlocal coupling and is included for completeness. Details on the implementation of the three types of couplings and corresponding first principles calculations of the parameters can be found in the methods section. We note here that the calculation of the nonlocal EPC is the step that requires the largest computation time of the approach (~10,000CPUh per material in dependence on the molecular size), but has the

advantage of using quantum-chemical methods that are transferable to new materials.

The timescale τ_{slow} in Eq. (6) is a crucial parameter defining the "lifetime" of the quasi-static disorder landscape. It is usually set to the inverse of the circular frequency $\tau_{slow} = \omega_{slow}^{-1}$ of the dominating vibrations, which can be, for example, extracted from molecular dynamics (MD) simulations[21]. To avoid costly ab initio MD simulations, we follow a different route and extract τ_{slow} from the mode-resolved disorder Eq. (2) based on the mode-resolved EPC. The disorder landscape is defined by both the disorder in the
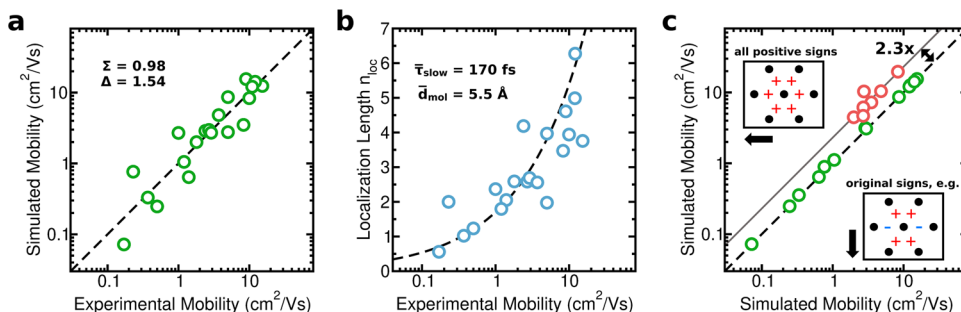
Fig. 4 Comparison of simulated and experimental hole mobilities. a Highest mobilities simulated in transport direction with the combined approach versus experimental mobilities. The black dotted line represents the case in which both coincide. **b** Experimental mobility versus the simulated localization length $n_{loc} = L_{loc}/d_{mol} \leq$ in transport direction in units of molecular center-of-mass distances d_{mol}. The black dotted line shows the dependency according to TL (Eq. (8)) using the stated averaged $\overline{\tau}_{slow}$ and $\overline{d}_{mol}$ values. **c** Simulated mobility using the original signs of the transfer integrals (x-axis) versus the simulated mobility by using all positive signs for the transfer integrals (y-axis). Materials that show a large increase of the mobility (of in average a factor of 2.3) due to the sign change are highlighted in red.

onsite-energies (with standard deviation σ_{MM}^2), caused by local and environmental EPC, and disorder in the transfer integrals (with standard deviation σ_{MN}^2), caused by nonlocal EPC. We thus extract ω_{slow} from the collective disorder strength using a weighted average (see methods section). The resulting values of τ_{slow} for the 20 crystals range from 60 fs to 270 fs and are summarized in Table 1. The average value over all compounds is about $\overline{\tau}_{slow} = 170$ fs, being of the same order of magnitude to the values obtained from MD simulations[21,22]. We note that their calculation via mode-resolved EPC allows the calculation of the ab initio parameters for new materials for which no force fields are available.

Studied materials and transport simulations

We assess the applicability of the combined approach by calculating the charge-carrier mobility at room temperature ($T = 300$K) using a set of 20 different organic semiconductor crystals and comparing them to known experimental mobilities. The molecular structures of the studied molecules are shown in Fig. 3. They include different classes of typical organic semiconductors, such as acenes, thiophenes, benzothiophenes, and some of their functionalized derivatives. The materials cover a broad range of ab initio parameters and experimental mobilities, ranging from $\mu_{PMSB} = 0.17$ cm^2/Vs for PMSB[41] to $\mu_{rubrene} = 15.3$ cm^2/Vs for rubrene[42]. The mobilities, as well as ab initio parameters are listed in Table 1.

While Eq. (6) enables the calculation of the mobility in any possible direction, here we focus on the maximum intrinsic mobility in transport direction. Figure 4a shows the computed mobilities μ_{sim} in comparison to the experimental mobilities μ_{exp}. The black dotted diagonal line is a guide for the eye, representing the ideal case $\mu_{exp} = \mu_{sim}$. We find that simulated and experimental mobilities correlate closely. This means that the simulation approach allows identifying low- and high- mobility organic crystals, which suggests that the approach could be used to estimate the charge-carrier mobility of new, unknown materials. We further quantify the correlation between simulation and experiment by calculating the ratio of both μ_{sim}^i/μ_{exp}^i for the 20 studied materials, and analyze its average $\Sigma = \exp(\frac{1}{n}\sum_i^n \ln(\mu_{sim}^i/\mu_{exp}^i))$ and the corresponding spread $\Delta = \exp(\frac{1}{n}\sum_i^n |\ln(\mu_{sim}^i/\mu_{exp}^i)|)$. We obtain $\Sigma = 0.98$ and $\Delta = 1.54$. That is, in average the simulated mobilities deviate by a factor of 1.54 (over- or underestimation) from the experimental mobilities, rendering the approach predictive.

Interestingly, we find that the present methodology, which is based on the coherent quantum diffusion, also yields good results for the low-mobility materials with $\mu \leq 1$ cm^2/Vs, although these are more likely in the hopping-transport regime that is driven by molecular vibrations. To explain this observation, we study the localization lengths L_{loc} from Eq. (6). For convenience, we use the

material dependent length unit d_{mol}, which is the center-of-mass distance between neighboring molecules with the largest transfer integral (see Table 1 for the numerical values). We define $n_{loc} = L_{loc}/d_{mol}$ as a measure for the number of molecules the wave-packet can approximately reach in transport direction during the time τ_{slow}. In Fig. 4b we plot this localization length n_{loc} against the experimental mobility for all 20 materials. As intuitively expected, the higher the mobility, the larger is the number of molecules the wave-packet delocalizes over[22]. As a guide for the eye, we also show the analytical dependency, which is obtained by resolving Eq. (6) for L_{loc} and use an averaged molecular distance of $\overline{d}_{mol} = 5.5$ Å and averaged relaxation time $\overline{\tau}_{slow} = 170$ fs:

$$n_{loc} = \sqrt{2k_BT\mu\overline{\tau}_{slow}/e}/\overline{d}_{mol}. \tag{8}$$

For materials with mobilities below 1 cm^2/Vs, n_{loc} is about one to two molecular distances. Thus, in this regime the TL approach can be interpreted to describe a hop of a localized wave-packet from one molecule to the other during the time τ_{slow} in analogy to hopping-transport simulations[31]. It is worth mentioning that, in contrast to hopping approaches, this observed behavior is not an a priori assumption but arises from the inability of the wave-packet to delocalize further than one neighboring molecule in transport direction due to strong disorder potentials. When focusing on the opposite limit, i.e. if one extrapolates Eq. (8) to estimate when a mobility of $\mu = 100$ cm^2/Vs could be reached, one would obtain a required delocalization to $n_{loc} = 17$.

A key proposal in the TL model is the dependency of L_{loc} (and the resulting charge-carrier mobility μ_{sim}) on the relative signs of the transfer integrals that occur between a molecule and its neighbors,[21] which is due to changes in the band structure when the sign of the transfer integrals change. This effect is explained in detail in Supplementary Note 2. For holes, a positive product of the signs of non-equivalent neighbors within the high-mobility plane would favor transport, whereas a negative product impedes transport.

To study this effect, we compare the simulated mobility using the original DFT-simulated signs (see methods section) with mobilities using all positive transfer integrals (APT) μ_{sim}^{APT} for all 20 materials in Fig. 4c (values in Table 1). For most of the materials, the change of the signs has only a minor effect (green circles). The reasons are either already existing ideal sign combinations (e.g. C10-DNBDT and C10-DNTT) or a strong tendency for 1D transport (e.g. BB-PTA and PMSB) in which other transfer integrals but the largest are of minor importance. For seven materials, we see a significant increase in the mobility by an average factor of 2.3 (orange circles). These are indeed materials that show only one transfer integral with negative sign within the high-mobility plane, yielding a negative sign product (e.g. for most of the acenes,
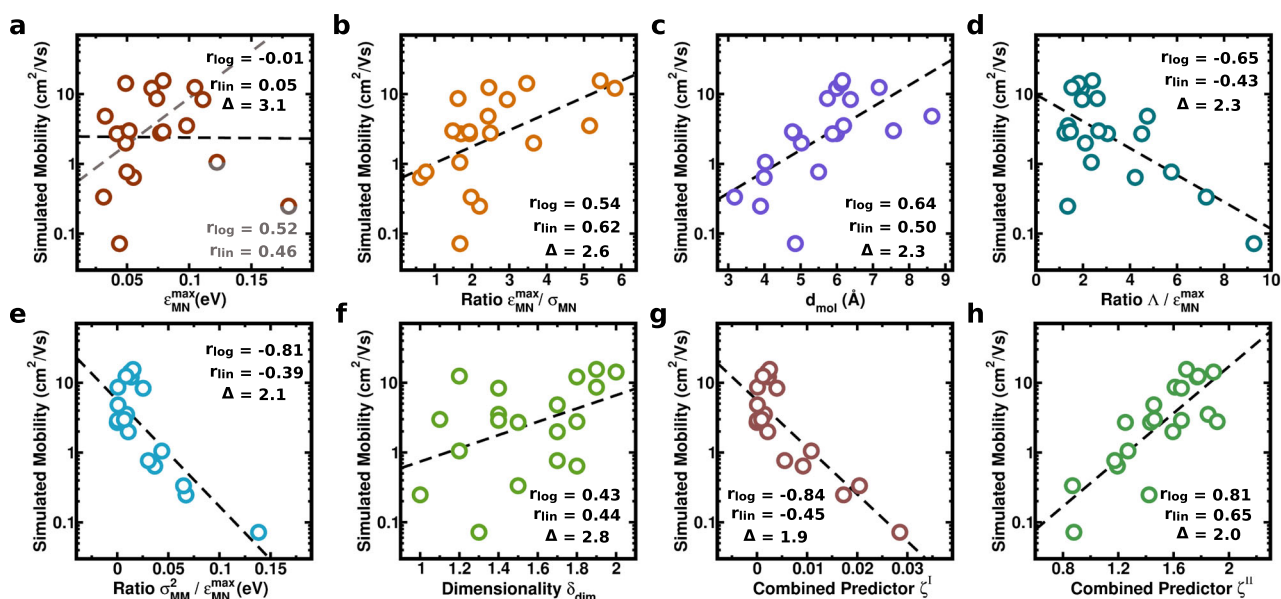
Fig. 5 Correlation between material parameters and the simulated mobility. We present the correlation coefficient with respect to the logarithmized mobility (r_{log}) and the original data (r_{lin}). The black dotted line is a linear fit between the studied material parameter and logarithmized mobility, while Δ is the average deviation from this fit. The fit details and fit parameters can be found in Supplementary Note 3. **a** shows the dependency of the simulated mobility on the maximum transfer integral ε_{MN}^{max}. Here, a second fit is performed by hypothetically neglecting two outliers (gray half circle), leading to the correlation shown in gray. The further studied parameters are **b** the ratio between the maximum transfer integral ε_{MN}^{max} and its nonlocal disorder σ_{MN}, **c** the molecular center-of-mass distance in the direction of the largest transfer integral d_{mol}, **d** the ratio between the reorganization energy Λ and transfer integral ε_{MN}^{max}, **e** the ratio between the local disorder σ_{MM}^2 and transfer integral ε_{MN}^{max}, and **f** the dimensionality δ_{dim}. The last plots show combinations of the previous predictors: the combined predictor ζ^I in **g**, and fast-to-calculate combined predictor ζ^{II} in **h**.

DNTT, DBTDT). Consequently, the relative signs of the transfer integrals can have a significant impact on the electronic structure and transport and should be considered when using transfer integrals as a material predictor.

Due to the variety of studied structures, it is also possible to analyze the correlation between simplified predictors and the simulated mobility. The reduction of the complexity of the transport simulation to predictors can improve the understanding of which parameters influence the mobility most. This knowledge is helpful as a guidance for design principles or can be used as a fast measure of transport capabilities in machine learning in the future, where a large number of structures have to be screened efficiently[43,44]. To analyze for possible dependencies, we graphically compare the dependency of the simulated mobility on different predictors in Fig. 5 and calculate the correlation coefficients r. Since the mobilities cover several orders of magnitude, while the predictors cover only one, we calculate the correlation to both the logarithmized mobility $\ln(\mu) \to r_{log}$ and original mobility $\mu \to r_{lin}$. We further present a linear fit of the predictor to $\ln(\mu)$ as black dashed line, which corresponds to the predicted mobility using solely this predictor and assuming an exponential dependency. The corresponding fit parameters can be found in Supplementary Note 3. Finally, the average spread around the prediction Δ (see above for the definition) is also shown. We first study obvious descriptors, like the transfer integral ε_{MN}^{max} and its disorder, which has been studied before by Troisi and coworkers[32], and then proceed to more complex descriptors to improve the predictability.

A first predictor is the maximum transfer integral ε_{MN}^{max} enabling electronic transport. As suggested by early hopping approaches, where the hopping rate is proportional to ε_{MN}^2, one might expect a distinct positive correlation between the simulated mobility and ε_{MN}^{max}. As shown in Fig. 5a, in contrast to the expectation, we observe a very weak correlation with $r_{lin} = 0.05$[32]. When hypothetically excluding the two most outlying data points of the

molecules BB-PTA and TTF-α (half gray circles), which show large transfer integrals ($\varepsilon_{MN}^{max} > 100$ meV) but small mobilities ($\mu \leq 1$ cm^2/Vs), we can indeed find a much stronger correlation of $r_{log} = 0.52$. Our analysis shows that, besides large transfer integrals, these two materials also show exceptionally large nonlocal and local disorders, which suggests that the mere transfer integral is unsuitable as a general predictor for the mobility. Therefore, we analyze a related one, namely the ratio between the maximum transfer integral ε_{MN}^{max} and the disorder σ_{MN} in the same (cf. Fig. 5b). We indeed find a correlation of $r_{lin} = 0.62$, while for the nonlocal disorder σ_{MN} alone we find a weaker correlation of $r_{log} = -0.41$ (not graphically shown). The reason that the combination of both parameters yields a good predictor is quite intuitive: the larger the transfer integral compared to the disorder, the better is the delocalization of the states and the larger are the localization length L_{loc} and the mobility.

A quantity that is directly connected to the localization length L_{loc} is the molecular center-of-mass distance d_{mol}. If all other parameters are constant, a larger d_{mol} directly increases L_{loc} since the charge carriers travel larger distances between molecules. In Fig. 5c, we compare the simulated mobility with d_{mol} in the direction of the largest transfer integral. Indeed, a good correlation of $r_{log} = 0.64$ can be found. This suggests that the molecular center-of-mass distance in transport direction is a good predictor for the mobility and should be optimized experimentally, e.g. via functionalization. A prominent example is rubrene where the large center-of-mass distance ($d_{mol} = 7.2$ Å) is caused by a special crystal packing that is induced by the functionalization of tetracene with phenyl side groups.

A popular transport parameter is the single-molecule reorganization energy Λ, which is a measure of the local EPC. It can be computed easily and enters into fast mobility estimations like Marcus theory[45,46]. In the present approach, the reorganization energy does not enter the mobility calculation, still we can check for possible correlations. The ratio $\Lambda/\varepsilon_{MN}^{max}$ is compared to the

carrier mobility in Fig. 5d and we observe a correlation with $r_{\log} = -0.65$. This is further improved in case of the ratio between the local disorder strength σ_{MM}^2 and the maximum transfer integral $\varepsilon_{MN}^{\max}$ (shown in Fig. 5e), exhibiting a strong correlation of $r_{\log} = -0.81$. We find the physical reason for this strong correlation of this quantity in the energetic distribution of the band-edge states. When the density-of-states approximately exhibits an exponential Urbach tail[47], the predictor $\sigma_{MM}^2/\varepsilon_{MN}^{\max}$ is closely related to the corresponding exponential steepness parameter, i.e. the Urbach Energy E_U[48]. A steeper exponential tail (low values of $\sigma_{MM}^2/\varepsilon_{MN}^{\max}$) means that the Fermi energy is closer to the band center, causing an increased contribution of delocalized states and thus larger charge-carrier mobilities.

The next predictor in our analysis is the dimensionality of transport. Materials showing 1D transport characteristics (e.g. by having only one set of equivalent neighbors with large transfer integrals) are not good transport materials, since they are prone to localization in case of static disorder due to limited percolation pathways[21,32]. Here, we measure the dimensionality of transport $\delta_{\dim}$ of the studied systems by analyzing the directional distribution of all transfer integrals to all nearest-neighbor molecules of a center molecule. We restricted ourselves to the distribution of transfer integrals within the high-mobility 2D plane (details on the calculation can be found in the methods section). Thus, $\delta_{\dim}$ can take on values between 1 (1D transport, i.e. only one large transfer integral in one direction) and 2 (2D transport, i.e. equally large transfer integrals within a 2D plane). Figure 5f shows the dependency of the simulated mobility on $\delta_{\dim}$. A correlation of $r_{\log} = 0.43$ is found, which is weaker than for the previous predictors. Still the dimensionality is worth considering when assessing the transport capability of new materials.

In a final analysis, we study if an even better correlation can be found by combining multiple predictors that correlate well with the simulated mobility. The first combination (shown in Fig. 5g) is $\sigma_{MM}^2/\varepsilon_{MN}^{\max}$ (the best predictor in Fig. 5e) and the molecular center-of-mass distance d_{mol} (the second-best predictor that does not depend on the local coupling, cf. Fig. 5c). Both predictors are combined via a product: $\zeta^I = \sigma_{MM}^2/(\varepsilon_{MN}^{\max} * d_{\mathrm{mol}})$. This combination shows a slightly higher correlation of $r_{\log} = -0.84$ compared to the sole predictor $\sigma_{MM}^2/\varepsilon_{MN}^{\max}$. The second combination focuses on fast-to-calculate, but less reliable predictors. We chose the ratio between reorganization energy and transfer integral $\Lambda/\varepsilon_{MN}^{\max}$ (Fig. 5d), the center-of-mass distance d_{mol} (Fig. 5c), and the dimensionality $\delta_{\dim}$ (Fig. 5f). Here, we obtained the best result by combining them via the geometric average $\zeta^{II} = \sqrt[3]{\varepsilon_{MN}^{\max} * d_{\mathrm{mol}} * \delta_{\dim}/\Lambda}$, which is shown in Fig. 5h. Indeed, the correlation of the combined predictor ζ^{II} ($r_{\log} = 0.81$) is better than the one of the individual terms. We thus suggest it as an easy-to-compute predictor for the mobility, which is more reliable than its sole components like the reorganization energy Λ or transfer integral $\varepsilon_{MN}^{\max}$.

The values of all studied predictors (Table 1) can be used to understand differences between the simulated mobilities of the studied materials, whereby we here pick out the most clear-cut cases for the discussion. C10-DNBDT and C10-DNTT for example show the highest simulated mobilities with medium transfer integrals (50–70 meV), whereas BB-PTA shows one of the lowest simulated mobilities despite having the largest transfer integral (180 meV). Therefore, the bare value of the transfer integral alone is no reliable predictor for the mobility. This weak correlation indicates that other factors, like the vibrations and EPC, are very important. For example, more relevant is the ratio between the transfer integral and the electronic disorder due to EPC. This is high for C10-DNBDT and C10-DNTT but low for BB-PTA, leading to stronger localization effects for the latter. For BB-PTA this effect is further enhanced due to the 1D-like transport channel induced by the crystal packing, where there are large transfer integrals to only

two nearest-neighbor molecules. This 1D channel makes BB-PTA prone to localization in analogy to the concept of conventional Anderson localization in disordered systems due to the lack of additional percolation pathways[49]. In contrast, C10-DNBDT and C10-DNTT have 2D high-mobility planes which are enforced by their core-alkyl-side-chain molecular structure, which opens up additional percolation pathways and makes them less susceptible to localization. Finally, the intermolecular distance of BB-PTA is by a factor of 1.5 smaller than for C10-DNBDT and C10-DNTT, directly reducing the distance the charge carriers can diffuse over. All these effects sum up in the simulation, leading to mobilities of BB-PTA that are factor of 50 smaller than for C10-DNBDT and C10-DNTT despite more-than-doubled transfer integrals. On top, the latter two molecules show ideal sign combinations of the transfer integrals (all positive transfer integrals), which maximizes the total bandwidth and producing the highest simulated mobilities.

In conclusion, we presented a framework to calculate the charge-carrier mobility of organic semiconductors by combining the quasi-static treatment of slow molecular vibrations (transient localization model) with the treatment of fast molecular vibrations from polaron theory. It is required, since the wide vibrational spectrum of organic molecules does not allow for a collective description of all modes in a single analytical treatment. The agreement between simulated and experimental mobilities for the full range of studied materials (quantified to an expected ratio of 1.54) suggests a good predictability for novel compounds. Using purely quantum-chemical methods to calculate the material parameters, the total computational expense is quite modest with about 15,000CPUh per material, where most of the computation time is required for the calculation of the nonlocal EPC. All simulations can be performed in parallel on high-performance computing clusters.

Finally, the correlation between the simulated mobility and simple predictors potentially allows estimating μ without performing all ab initio calculations. Since multiple parameters enter the transport simulation, there are also several predictors that correlate with the mobility. While the maximum transfer integral $\varepsilon_{MN}^{\max}$ was shown to fail as a predictor for certain materials, there are several alternatives that work well such as the dimensionality of transport $\delta_{\dim}$ or the center-of-mass distance to the neighboring molecule with the largest transfer integral d_{mol}. The tightest correlations among all predictors showed r values between 0.64 and 0.81. The best predictor was the ratio $\sigma_{MM}^2/\varepsilon_{MN}^{\max}$ between the local disorder strength and largest transfer integral, which requires only low computational resources due the absence of nonlocal EPC. To further increase the predictability, not a single but a set of predictors can be used. From our analysis, we suggest the geometric average of an easy-to-calculate set of predictors: (i) the ratio between reorganization energy Λ and the maximum transfer integral $\varepsilon_{MN}^{\max}$ (ii) the dimensionality $\delta_{\dim}$ and (iii) the center-of-mass distance d_{mol}. While these predictors cannot reach the predictability of the full mobility simulations with ab initio parameters, they are fast to calculate and can be applied to estimate the mobility for a much larger set of systems in the future.

METHODS
Transfer integrals
The transfer integrals were calculated within the fragment-orbital approach[50,51] for molecular dimer pairs in a 3D nearest-neighbor shell of a given central molecule. Including Löwdin orthogonalization[52], they are defined as

$$\varepsilon_{MN} = \langle \phi_M | S^{-1} F S^{-1} | \phi_N \rangle \tag{9}$$

The matrix F, overlap matrix S and molecular Kohn-Sham orbitals ϕ_M (corresponding to the highest occupied molecular HOMO orbital in case of hole transport) were calculated with density

functional theory (DFT). To this end, the B3LYP exchange-correlation functional[53,54] and 6–311 G** basis set[55,56] were used within the Gaussian 16 program package[57].

The signs of the transfer integrals were obtained via comparison to the signs between maximally localized Wannier functions[58] that were obtained with the Wannier90 code[59,60] in combination with the VASP package[61,62] using a plane-wave basis set. The calculations were based on the projector augmented-wave method[63,64] and PBE functional[65,66]. Depending on the number of molecules in the unit cell, two or four valence bands were used for the wannierization to obtain the sign.

Vibrational analysis

The local coupling was calculated with DFT using the vibrational modes of a single, isolated gas-phase molecule. The mode energy and displacement patterns were obtained using the normal mode analysis as implemented in Gaussian 16[57] using the B3LYP exchange-correlation functional[53,54] and 6–311 G** basis set[55,56].

The nonlocal and environmental coupling is based on the vibrational crystal modes. Due to the increased system size, the calculation was performed with density functional tight binding (DFTB)[67] instead of DFT. It has been shown that, while DFTB is not perfectly suited for the calculation of electronic properties, it describes vibrational properties sufficiently well[68]. The normal mode analysis was performed for unit cells consisting of, in general, 8 molecules and periodic boundary conditions. The specific choice of the supercell size ensures, that the supercell includes one of the two equivalent nearest neighbor molecules of the 3D shell for which we calculated the transfer integrals. Thus, we include symmetric ($q = 0$, phase between adjacent molecules is $e^{iqa} = 1$) and anti-symmetric ($q = \frac{\pi}{a}$, phase between adjacent molecules is $e^{iqa} = -1$) vibrations. More q points could in principle be sampled by further increasing the unit cell size[68,69], but drastically increases the computational load.

For four molecules (rubrene, C10-DNBDT, C10-DNTT, and TIPS-pentacene) we included only 4 molecules in the unit cell due to the large molecular and unit cell size. We included the nearest-neighbor molecules, corresponding to two sampled q-points, within the high-mobility plane. Consequently, in the third low-mobility direction, we included only the symmetric vibrations ($q = 0$, $e^{iqa} = 1$).

The crystal mode analysis was performed with third order DFTB[70] implemented in the DFTB+ program package[70,71] using the *3ob* parameter sets[70]. For TIPS-Pentacene, the *pbc*[72] parameter sets, which include silicon, were used. Additionally, Grimme's dispersion correction GD3[73] was included in every calculation.

To compensate numerical errors in the mode frequencies occurring during normal mode analysis, which are most impactful for the low-frequency modes, the frequencies obtained from the normal analysis were re-computed. This is done by calculating the second derivative of the DFTB crystal energy $E_{\text{DFTB}}^{\text{Crystal}}(X_Q)$ in dependence on the deflection X_Q. The new frequencies are obtained as:

$$\omega_Q = \sqrt{\frac{\partial^2 E_{\text{DFTB}}^{\text{Crystal}}(X_Q)}{\partial X_Q^2}} \tag{10}$$

If negative frequencies were obtained for (non-translational) crystal modes, the crystal was shuffled according to these modes, followed by a second relaxation and frequency calculation. In rare cases, very small but non-negative mode frequencies ($<5\,\text{cm}^{-1}$) remained. These modes fully contributed to the disorder potential in Eq. (2) but were suppressed in the calculation of τ_{slow} in Eq. (15).

Calculation of electron–phonon coupling

The local coupling g_{MM}^Q, nonlocal coupling g_{MN}^Q and environmental coupling $g_{MM}^{Q,CF}$, collectively notated as G^Q, were calculated using the deflection of the normal modes X_Q and mode energies ω_Q

according to:

$$G^Q = \frac{\partial E(X_Q)}{\partial X_Q} \frac{1}{\sqrt{2\omega_Q^3 \hbar}} \tag{11}$$

The derivative is calculated in the frozen-phonon approach[74] and the energy E in Eq. (11) stands for the onsite energy ε_M (local coupling), the transfer integral ε_{MN} (nonlocal coupling) and the electrostatic interaction energy of the charge carrier with the surrounding molecules E_{CF}^M. The calculations of the respective energies are performed in real-space to ensure scalability to larger molecules, since the required DFT simulations can then be performed for smaller subsystems.

Onsite energies and local coupling

The onsite energies, corresponding to the binding energy of the charge carrier in the HOMO orbital in case of hole transport, is calculated as[75]:

$$\varepsilon_{MM} \stackrel{!}{=} IP = E_{\text{DFT}}^0 - E_{\text{DFT}}^+, \tag{12}$$

where $E_{\text{DFT}}^{0/+}$ is the total DFT energy for the neutral or positively charged molecule, respectively. The energies are calculated with the B3LYP functional[53,54] and the 6–311 G** basis set[55,56] in Gaussian 16[57].

In gas phase, the molecules TTF, DT-TTF, and HM-TTF show very large local coupling constants for low-frequency bending modes (and consequently large reorganization energies), which are not present to that extent in a crystalline environment. To account for the constraints within the crystal, we calculated the reorganization energy in a cluster environment using the well-established 4-point method[76]. The cluster included all nearest-neighbor molecules of a central molecule that is allowed to relax. The atomic positions of the neighbor molecules were kept constant, while the charging states of the central molecule were controlled via charge constraints. These calculations were performed with the NWchem package[77] on the level of theory presented above. The mode-resolved electron-phonon couplings of these molecules were scaled down, so that twice the total polaron binding energy (relaxation energy) $E_{\text{pol}} = \sum_Q \hbar \omega_Q \left| g_{MM}^Q \right|^2$ is equal to the reorganization energy obtained within the cluster environment.

Nonlocal coupling

The transfer integrals ε_{MN} used to calculate the nonlocal coupling according to Eq. (11) have been calculated similar to Eq. (9), however the DFT calculations were performed using the smaller 6–31 G* basis set instead of 6–311 G** to reduce the computational load. Further, we used a method proposed by Landi et al.[78] to calculate the derivatives $\frac{\partial \varepsilon_{MN}(X_Q)}{\partial X_Q}$ more efficiently. For a unit cell consisting of $N = n_{\frac{\text{mol}}{\text{unit}}} * n_{\frac{\text{atom}}{\text{mol}}}$ there are $3N$ normal modes, for which the derivative in Eq. (11) has to be performed. However, only $2*n_{\frac{\text{atom}}{\text{mol}}}$ atoms contribute to the transfer integral ε_{MN}. Thus, the derivative with respect to the full displacement pattern is replaced by a derivative with respect to only the displacement s of the atoms l in direction a contributing to the transfer integral weighted with the displacement pattern e_Q^a of mode Q:

$$\frac{\partial \varepsilon_{MN}(X_Q)}{\partial X_Q} = \sum_{al} e_Q^{al} \frac{\partial \varepsilon_{MN}(s_a^l)}{\partial s_a^l} \tag{13}$$

As a consequence, only $3 * 2 * n_{\frac{\text{atom}}{\text{mol}}}$ derivatives have to be computed. In our case, this treatment saves computational time of a factor of $n_{\frac{\text{mol}}{\text{unit}}}/2 = 4$.

Electrostatic interaction energy and environmental coupling

The final type of electron-phonon coupling is the environmental coupling arising due to changes in the electrostatic interaction energy between the charge carrier and the crystal field generated

by the surrounding molecules E_{CF}. Although the surrounding molecules are neutral, the interaction energy is nonzero due to non-vanishing quadrupole moments, and, for some molecules, non-vanishing dipole moments. For the calculation, the charge carrier is approximately localized on a single molecule M[76]. The interaction energy of the electronic charge distribution is modeled by atomic point charges q[75,76] obtained by an electrostatic potential fit (ESP)[79,80] and reads

$$E_{CF}^{M} = \frac{1}{4\pi\epsilon_0} \sum_i^M \sum_j^{env} \frac{\Delta q_i \cdot q_j}{\epsilon|\mathbf{R}|}. \tag{14}$$

The sum over i goes over all atomic point charges of the excess charge carrier $\Delta q_i = q_i^+ - q_i^0$ localized on site M and the sum over j goes over all atomic point charges of the neutral molecular environment. $|\mathbf{R}| = |\mathbf{r}_i - \mathbf{r}_j|$ is the distance between both charges. ϵ_0 is the vacuum permittivity and ϵ is the relative (isotropic) permittivity of the medium. It is set to $\epsilon = 3.6$ for all materials, which is a common (average) value for organic semiconductors. We note that the environmental coupling is the smallest disorder contribution compared to the nonlocal coupling and is included in this approximated fashion for numerical efficiency and completeness.

Relaxation time

In the TL approach, the relaxation time is set to the timescale of the slow quasi-static modes τ_{slow} on which the quasi-static disorder landscape changes. It is set to the inverse of the circular frequency of a dominating low-frequency mode $\tau_{slow} = \omega_{slow}^{-1}$. Here, the disorder landscape consists of two contributions: the local disorder σ_{MM} and nonlocal disorder σ_{MN}. Thus, we extract the dominating frequency from the combined disorder $\sigma_{MM}^2 + \sum_{MN} \sigma_{MN}^2$ (for a given center molecule M and nearest-neighbors N) in a weighted average:

$$\tau_{slow} = \left(\frac{\sigma_{MM}^2 + \sum_N \sigma_{MN}^2}{\sum_Q^{slow} \hbar^2 \omega_Q \left(\sum_N |g_{MN}^Q|^2 + |g_{MM}^Q|^2 \right)(1 + 2N_Q)} \right)^{-1}$$
$$= \left(\frac{\sum_Q^{slow} (\hbar\omega_Q)^2 \left(\sum_N |g_{MN}^Q|^2 + |g_{MM}^Q|^2 \right)(1 + 2N_Q)}{\sum_Q^{slow} \hbar^2 \omega_Q \left(\sum_N |g_{MN}^Q|^2 + |g_{MM}^Q|^2 \right)(1 + 2N_Q)} \right)^{-1} \tag{15}$$

Charge transport simulations

The charge-carrier mobilities are calculated according to Eq. (6) of the main text and are based on the time- and energy-resolved quantum spread of Eq. (7) of the main text:

$$\Delta X^2(E, t) = \frac{\langle \Phi'_{RP}(t) | \delta(E - H) | \Phi'_{RP}(t) \rangle}{\langle \Phi_{RP} | \delta(E - H) | \Phi_{RP} \rangle}, \tag{16}$$

with $|\Phi'_{RP}(t)\rangle = [X, U(t)]|\Phi_{RP}\rangle$, $U(t) = e^{-iHt/\hbar}$. The energy-projection and time-evolution is performed with respect to the purely electronic Hamiltonian in Eq. (4) of the main text. To this end, we build a 3D model Hamiltonian consisting of 12,288,000 sites for each material. The system is initialized in a random-phase state[81] $|\Phi_{RP}\rangle = N_{sites}^{-1/2} \sum_j^{sites} e^{i\theta_j} |\Phi_j\rangle$, i.e. a state having a different random phase θ_j for each site j. This allows us to simulate the quantum spread in Eq. (7) of the main text as an average over different disorder landscapes in different parts of the 3D sample in a single run since the wave-packet localizes in only a small region of the full 3D sample. The energy projection in Eq. (16) is performed using the Lanczos algorithm[82], while the time-evolution is performed using the Chebyshev-polynomial expansion[83].

Estimation of the dimensionality

The dimensionality is studied by analyzing the directional distribution of all transfer integrals to all nearest-neighbor molecules of a given center molecule. We therefore establish a standardized, orthonormal frame: the vector $\mathbf{e}_x$ points in the direction of the largest transfer integral, $\mathbf{e}_y$ lies in the plane spanned by the vectors in direction of the two largest transfer integrals and is chosen to be perpendicular to $\mathbf{e}_x$, and $\mathbf{e}_z$ is perpendicular to both $\mathbf{e}_x$ and $\mathbf{e}_y$. We now calculate the averaged nearest-neighbor transfer integral $\bar{\varepsilon}_{OP}^a$ (for a given center molecule O) in direction a in a weighted average, whereby the weight is the projection of the center-of-mass distance vector $\mathbf{d}_{OP}$ onto $\mathbf{e}_a$:

$$\bar{\varepsilon}_{OP}^a = \frac{\sum_P \varepsilon_{OP} \mathbf{d}_{OP} \mathbf{e}_a}{\sum_P \mathbf{d}_{OP} \mathbf{e}_a} \tag{17}$$

the sum runs over all nearest-neighbor molecules P. To study the two-dimensionality as done in the main manuscript, we take the sum $\bar{\varepsilon}_{OP}^x$ and $\bar{\varepsilon}_{OP}^y$, which is the sum of the averaged transfer integrals within the high-mobility plane, and normalize it to the maximum transfer integral:

$$\delta_{dim}^{2D} = \frac{(\bar{\varepsilon}_{OP}^x + \bar{\varepsilon}_{OP}^y)}{\max(\bar{\varepsilon}_{OP}^x, \bar{\varepsilon}_{OP}^y)} \tag{18}$$

This choice ensures that δ_{dim}^{2D} equals to one if there are strong contributions of transfer integrals in only one direction (i.e. 1D transport), while it is two if there are equal contributions into two orthogonal directions within the high-mobility plane (i.e. 2D transport).

REFERENCES

1. Brown, A. R., Pomp, A., Hart, C. M. & De Leeuw, D. M. Logic gates made from polymer transistors and their use in ring oscillators. *Science* **270**, 972–974 (1995).
2. Gershenson, M. E., Podzorov, V. & Morpurgo, A. F. Colloquium: electronic transport in single-crystal organic transistors. *Rev. Mod. Phys.* **78**, 973–989 (2006).
3. Briseno, A. L. et al. Patterning organic single-crystal transistor arrays. *Nature* **444**, 913–917 (2006).
4. Mei, J., Diao, Y., Appleton, A. L. & Bao, Z. Integrated materials design of organic semiconductors for field-effect transistors. *J. Am. Chem. Soc.* **135**, 6724–6746 (2013).
5. Kippelen, B. & Brédas, J. L. Organic photovoltaics. *Energy Environ. Sci.* **2**, 251–261 (2009).
6. Cao, W. & Xue, J. Recent progress in organic photovoltaics: device architecture and optical design. *Energy Environ. Sci.* **7**, 2123–2144 (2014).
7. Meng, L. et al. Organic and solution-processed tandem solar cells with 17.3% efficiency. *Science* **361**, 1094–1098 (2018).
8. Berggren, M. et al. Light-emitting diodes with variable colours from polymer blends. *Nature* **372**, 444–446 (1994).
9. Forrest, S. R. The road to high efficiency organic light emitting devices. *Org. Electron.* **4**, 45–48 (2003).
10. Reineke, S., Thomschke, M., Lüssem, B. & Leo, K. White organic light-emitting diodes: status and perspective. *Rev. Mod. Phys.* **85**, 1245–1293 (2013).
11. Holstein, T. Studies of polaron motion part I. The molecular-crystal model. *Ann. Phys.* **8**, 325–342 (1959).
12. Holstein, T. Studies of polaron motion: Part II. The "small" polaron. *Ann. Phys.* **8**, 343–389 (1959).
13. Hannewald, K. et al. Theory of polaron bandwidth narrowing in organic molecular crystals. *Phys. Rev. B* **69**, 075211 (2004).
14. Troisi, A. & Orlandi, G. Charge-transport regime of crystalline organic semiconductors: diffusion limited by thermal off-diagonal electronic disorder. *Phys. Rev. Lett.* **96**, 086601 (2006).
15. Ortmann, F., Bechstedt, F. & Hannewald, K. Charge transport in organic crystals: theory and modelling. *Phys. Status Solidi Basic Res.* **248**, 511–525 (2011).
16. Ishii, H., Honma, K., Kobayashi, N. & Hirose, K. Wave-packet approach to transport properties of carrier coupled with intermolecular and intramolecular vibrations of organic semiconductors. *Phys. Rev. B* **85**, 245206 (2012).

17. Heiber, M. C., Baumbach, C., Dyakonov, V. & Deibel, C. Encounter-limited charge-carrier recombination in phase-separated organic semiconductor blends. *Phys. Rev. Lett.* **114**, 136602 (2015).

18. Spencer, J., Gajdos, F. & Blumberger, J. FOB-SH: fragment orbital-based surface hopping for charge carrier transport in organic and biological molecules and materials. *J. Chem. Phys.* **145**, 064102 (2016).

19. Massé, A. et al. Ab initio charge-carrier mobility model for amorphous molecular semiconductors. *Phys. Rev. B* **93**, 195209 (2016).

20. Yi, H. T., Gartstein, Y. N. & Podzorov, V. Charge carrier coherence and Hall effect in organic semiconductors. *Sci. Rep.* **6**, 23650 (2016).

21. Fratini, S., Ciuchi, S., Mayou, D., Trambly de Laissardière, G. & Troisi, A. A map of high-mobility molecular semiconductors. *Nat. Mater.* **16**, 998–1002 (2017).

22. Giannini, S. et al. Quantum localization and delocalization of charge carriers in organic semiconducting crystals. *Nat. Commun.* **10**, 3843 (2019).

23. Roosta, S., Ghalami, F., Elstner, M. & Xie, W. Efficient surface hopping approach for modeling charge transport in organic semiconductors. *J. Chem. Theory Comput.* **18**, 1264 (2022).

24. Chang, B. K., Zhou, J. J., Lee, N. E. & Bernardi, M. Intermediate polaronic charge transport in organic crystals from a many-body first-principles approach. *npj Comput. Mater.* **8**, 63 (2022).

25. Carof, A., Giannini, S. & Blumberger, J. How to calculate charge mobility in molecular materials from surface hopping non-adiabatic molecular dynamics-beyond the hopping/band paradigm. *Phys. Chem. Chem. Phys.* **21**, 26368–26386 (2019).

26. Ortmann, F., Bechstedt, F. & Hannewald, K. Theory of charge transport in organic crystals: Beyond Holstein's small-polaron model. *Phys. Rev. B* **79**, 235206 (2009).

27. Troisi, A. & Orlandi, G. Dynamics of the intermolecular transfer integral in crystalline organic semiconductors. *J. Phys. Chem. A* **110**, 4065–4070 (2006).

28. Vukmirović, N., Bruder, C. & Stojanović, V. M. Electron-phonon coupling in crystalline organic semiconductors: Microscopic evidence for nonpolaronic charge carriers. *Phys. Rev. Lett.* **109**, 126407 (2012).

29. Troisi, A. Quantum dynamic localization in the Holstein Hamiltonian at finite temperatures. *Phys. Rev. B - Condens. Matter Mater. Phys.* **82**, 245202 (2010).

30. Fratini, S., Mayou, D. & Ciuchi, S. The transient localization scenario for charge transport in crystalline organic materials. *Adv. Funct. Mater.* **26**, 2292–2315 (2016).

31. Hutsch, S., Panhans, M. & Ortmann, F. Time-consistent hopping transport with vibration-mode-resolved electron-phonon couplings. *Phys. Rev. B* **104**, 054306 (2021).

32. Nematiaram, T., Padula, D., Landi, A. & Troisi, A. On the largest possible mobility of molecular semiconductors and how to achieve it. *Adv. Funct. Mater.* **30**, 2001906 (2020).

33. Fetherolf, J. H., Golež, D. & Berkelbach, T. C. A unification of the holstein polaron and dynamic disorder pictures of charge transport in organic crystals. *Phys. Rev. X* **10**, 021062 (2020).

34. Fan, Z. et al. Linear scaling quantum transport methodologies. *Phys. Rep.* **903**, 1–69 (2021).

35. Panhans, M. & Ortmann, F. Efficient time-domain approach for linear response functions. *Phys. Rev. Lett.* **127**, 016601 (2021).

36. Mahan, G. D. *Many-Particle Physics* (Kluwer Academic/Plenum Publishers, 2000).

37. Sánchez-Carrera, R. S., Paramonov, P., Day, G. M., Coropceanu, V. & Brédas, J. L. Interaction of charge carriers with lattice vibrations in oligoacene crystals from naphthalene to pentacene. *J. Am. Chem. Soc.* **132**, 14437–14446 (2010).

38. Lang, I. G. & Firsov, Y. A. Kinetic theory of semiconductors with low mobility. *Sov. Phys. JETP* **16**, 1301 (1963).

39. Kubo, R. Statistical-mechanical theory of irreversible processes. i. general theory and simple applications to magnetic and conduction problems. *J. Phys. Soc. Jpn* **12**, 570–586 (1957).

40. Nematiaram, T., Ciuchi, S., Xie, X., Fratini, S. & Troisi, A. Practical computation of the charge mobility in molecular semiconductors using transient localization theory. *J. Phys. Chem. C* **123**, 6989–6997 (2019).

41. Nakanotani, H., Saito, M., Nakamura, H. & Adachi, C. Highly balanced ambipolar mobilities with intense electroluminescence in field-effect transistors based on organic single crystal oligo(p -phenylenevinylene) derivatives. *Appl. Phys. Lett.* **95**, 033308 (2009).

42. Sundar, V. C. et al. Elastomeric transistor stamps: reversible probing of charge transport in organic crystals. *Science* **303**, 1644–1646 (2004).

43. Kunkel, C., Schober, C., Margraf, J. T., Reuter, K. & Oberhofer, H. Finding the right bricks for molecular legos: a data mining approach to organic semiconductor design. *Chem. Mater.* **31**, 969–978 (2019).

44. Kunkel, C., Margraf, J. T., Chen, K., Oberhofer, H. & Reuter, K. Active discovery of organic semiconductors. *Nat. Commun.* **12**, 2422 (2021).

45. Marcus, R. A. On the theory of oxidation-reduction reactions involving electron transfer. I. *J. Chem. Phys.* **24**, 966–978 (1956).

46. Marcus, R. A. & Sutin, N. Electron transfers in chemistry and biology. *Biochim. Biophys. Acta* **811**, 265–322 (1985).

47. Urbach, F. The long-wavelength edge of photographic sensitivity and of the electronic absorption of solids. *Phys. Rev.* **92**, 1324–1324 (1953).

48. Cohen, M. H. & Economou, E. N. Theory of electron band tails and the urbach optical-absorption edge. *Phys. Rev. Lett.* **57**, 1777–1780 (1986).

49. Anderson, P. W. Absence of diffusion in certain random lattices. *Phys. Rev.* **109**, 1492 (1958).

50. Valeev, E. F., Coropceanu, V., Da Silva Filho, D. A., Salman, S. & Brédas, J. L. Effect of electronic polarization on charge-transport parameters in molecular organic semiconductors. *J. Am. Chem. Soc.* **128**, 9882–9886 (2006).

51. Kirkpatrick, J. An approximate method for calculating transfer integrals based on the ZINDO Hamiltonian. *Int. J. Quant. Chem.* **108**, 51–56 (2008).

52. Löwdin, P. O. On the non-orthogonality problem connected with the use of atomic wave functions in the theory of molecules and crystals. *J. Chem. Phys.* **18**, 365–375 (1950).

53. Becke, A. D. Density-functional exchange-energy approximation with correct asymptotic behavior. *Phys. Rev. A* **38**, 3098–3100 (1988).

54. Lee, C., Yang, W. & Parr, R. G. Development of the Colle-Salvetti correlation-energy formula into a functional of the electron density. *Phys. Rev. B* **37**, 785–789 (1988).

55. Krishnan, R., Binkley, J. S., Seeger, R. & Pople, J. A. Self-consistent molecular orbital methods. XX. A basis set for correlated wave functions. *J. Chem. Phys.* **72**, 650–654 (1980).

56. McLean, A. D. & Chandler, G. S. Contracted Gaussian basis sets for molecular calculations. I. Second row atoms, Z=11-18. *J. Chem. Phys.* **72**, 5639–5648 (1980).

57. Frisch, M. J. et al. *G16_C01. Gaussian 16, Revision C.01* (Gaussian, Inc., Wallin, 2016).

58. Marzari, N., Mostofi, A. A., Yates, J. R., Souza, I. & Vanderbilt, D. Maximally localized Wannier functions: theory and applications. *Rev. Mod. Phys.* **84**, 1419 (2012).

59. Pizzi, G. et al. Wannier90 as a community code: new features and applications. *J. Phys. Condens. Matter* **32**, 165902 (2020).

60. Mostofi, A. A. et al. An updated version of wannier90: a tool for obtaining maximally-localised Wannier functions. *Comput. Phys. Commun.* **185**, 2309–2310 (2014).

61. Kresse, G. & Hafner, J. Ab initio molecular dynamics for liquid metals. *Phys. Rev. B* **47**, 558 (1993).

62. Kresse, G. & Furthmüller, J. Efficient iterative schemes for ab initio total-energy calculations using a plane-wave basis set. *Phys. Rev. B* **54**, 11169–11186 (1996).

63. Blöchl, P. E. Projector augmented-wave method. *Phys. Rev. B* **50**, 17953–17979 (1994).

64. Kresse, G. & Joubert, D. From ultrasoft pseudopotentials to the projector augmented-wave method. *Phys. Rev. B* **59**, 1758–1775 (1999).

65. Perdew, J. P., Burke, K. & Ernzerhof, M. Generalized gradient approximation made simple. *Phys. Rev. Lett.* **77**, 3865–3868 (1996).

66. Perdew, J. P., Burke, K. & Ernzerhof, M. Erratum: generalized gradient approximation made simple. *Phys. Rev. Lett.* **78**, 1396 (1997).

67. Elstner, M. & Seifert, G. Density functional tight binding. *Philos. Trans. R. Soc. A Math. Phys. Eng. Sci.* **372**, 20120483 (2014).

68. Xie, X., Santana-Bonilla, A. & Troisi, A. Nonlocal electron-phonon coupling in prototypical molecular semiconductors from first principles. *J. Chem. Theory Comput.* **14**, 3752–3762 (2018).

69. Yi, Y., Coropceanu, V. & Brédas, J. L. Nonlocal electron-phonon coupling in the pentacene crystal: Beyond the Γ-point approximation. *J. Chem. Phys.* **137**, 164303 (2012).

70. Gaus, M., Goez, A. & Elstner, M. Parametrization and benchmark of DFTB3 for organic molecules. *J. Chem. Theory Comput.* **9**, 338–354 (2013).

71. Hourahine, B. et al. DFTB+, a software package for efficient approximate density functional theory based atomistic simulations. *J. Chem. Phys.* **152**, 124101 (2020).

72. Rauls, E., Elsner, J., Gutierrez, R. & Frauenheim, T. Stoichiometric and non-stoichiometric (10$\bar{1}$0) and (11$\bar{2}$0) surfaces in 2H-SiC: a theoretical study. *Solid State Commun* **111**, 459–464 (1999).

73. Grimme, S., Antony, J., Ehrlich, S. & Krieg, H. A consistent and accurate ab initio parametrization of density functional dispersion correction (DFT-D) for the 94 elements H-Pu. *J. Chem. Phys.* **132**, 154104 (2010).

74. Giustino, F. Electron-phonon interactions from first principles. *Rev. Mod. Phys.* **89**, 015003 (2017).

75. D'Avino, G. et al. Electrostatic phenomena in organic semiconductors: fundamentals and implications for photovoltaics. *J. Phys. Condens. Matter* **28**, 433002 (2016).

76. Rühle, V. et al. Microscopic simulations of charge transport in disordered organic semiconductors. *J. Chem. Theory Comput.* **7**, 3335–3345 (2011).

77. Valiev, M. et al. NWChem: a comprehensive and scalable open-source solution for large scalemolecular simulations. *Comput. Phys. Commun* **181**, 1477–1489 (2010).

78. Landi, A. & Troisi, A. Rapid evaluation of dynamic electronic disorder in molecular semiconductors. *J. Phys. Chem. C* **122**, 18336–18345 (2018).

79. Singh, U. C. & Kollman, P. A. An approach to computing electrostatic charges for molecules. *J. Comput. Chem.* **5**, 129–145 (1984).

80. Besler, B. H., Merz, K. M. & Kollman, P. A. Atomic charges derived from semi-empirical methods. *J. Comput. Chem.* **11**, 431–439 (1990).

81. Iitaka, T. & Ebisuzaki, T. Random phase vector for calculating the trace of a large matrix. *Phys. Rev. E* **69**, 4 (2004).

82. Lanczos, C. An iteration method for the solution of the eigenvalue problem of linear differential and integral operators 1. *J. Res. Natl. Bur. Stand.* **45**, 2133 (1950).
83. Weiße, A., Wellein, G., Alvermann, A. & Fehske, H. The kernel polynomial method. *Rev. Mod. Phys.* **78**, 275–306 (2006).

AUTHOR CONTRIBUTIONS

S.H. and M.P. developed the theoretical model. S.H. performed the ab-initio calculations and transport simulations. F.O. supervised the project. The manuscript was written by all co-authors.

COMPETING INTERESTS

The authors declare no competing interests.

ADDITIONAL INFORMATION

Supplementary information The online version contains supplementary material available at https://doi.org/10.1038/s41524-022-00915-3.

Correspondence and requests for materials should be addressed to Frank Ortmann.

Reprints and permission information is available at http://www.nature.com/reprints

Publisher's note Springer Nature remains neutral with regard to jurisdictional claims in published maps and institutional affiliations.